



1 **Secondary Organic Aerosols Derived from Intermediate Volatility**

2 **n-Alkanes Adopt Low Viscous Phase State**

3 Tommaso Galeazzo¹, Bernard Aumont², Marie Camredon², Richard Valorso², Yong B. Lim³,

4 Paul J. Ziemann^{4,5}, and Manabu Shiraiwa^{1,*}

5

6

7 1. Department of Chemistry, University of California, Irvine, CA92625, USA

8 2. Univ Paris Est Creteil and Université Paris Cité, CNRS, LISA, F-94010 Créteil, France

9 3. California Air Resources Board, Riverside, CA92507, USA

10 4. Department of Chemistry, University of Colorado, Boulder, Colorado, USA

11 5. Cooperative Institute for Research in Environmental Sciences (CIRES), University of

12 Colorado, Boulder, Colorado, USA

13

14

15 * Correspondence to: m.shiraiwa@uci.edu

16

17



18 **Abstract.**

19 Secondary organic aerosol (SOA) derived from n-alkanes, as emitted from vehicles and volatile
20 chemical products, is a dominant component of anthropogenic particulate matter, yet its
21 chemical composition and phase state are poorly understood and hardly constrained in aerosol
22 models. Here we provide a comprehensive analysis of n-alkane SOA by explicit chemistry
23 modeling, machine learning, and laboratory experiments to show that, counterintuitively, n-
24 alkane SOA adopt low viscous semisolid or liquid states. Our study underlines the complex
25 interplay of molecular composition and SOA viscosity: n-alkane SOA with higher carbon
26 number mostly consists of less functionalized first-generation products with lower viscosity,
27 while the lower carbon number SOA contains more functionalized multigeneration products
28 with higher viscosity. This study opens up a new avenue for analysis of SOA processes and the
29 results indicate little kinetic limitations of mass accommodation in SOA formation, supporting
30 the application of equilibrium partitioning for simulating n-alkane SOA formation in large-
31 scale atmospheric models.

32

33 **Introduction**

34 Secondary organic aerosols (SOA) are ubiquitous in the atmosphere, affecting climate, air
35 quality and public health (Pöschl and Shiraiwa, 2015; Jimenez et al., 2009). They are generally
36 formed by multigenerational oxidation of volatile organic compounds (VOCs) emitted by both
37 anthropogenic and biogenic sources followed by condensation of semi-volatile oxidation
38 products into the particle phase (Ziemann and Atkinson, 2012; Kroll and Seinfeld, 2008). As
39 an important class of SOA precursors, there is a growing attention to intermediate volatile
40 organic compounds (IVOCs), which can partition to the gas phase upon dilution of primary
41 organic aerosols after fresh emission sources such as vehicle tailpipes, combustion of fossil and
42 fuel oils, and volatile chemical products (Robinson et al., 2007; McDonald et al., 2018). The
43 inclusion of IVOCs in the model simulations helps to reduce the gap between model simulation
44 and field observation of SOA (De Gouw et al., 2011; Li et al., 2022; Zhao et al., 2016).

45 SOA can adopt different particle phase states (liquid, amorphous semisolid, and glassy
46 solid), depending on its chemical composition, relative humidity and temperature (Virtanen et
47 al., 2010; Petters et al., 2019; Reid et al., 2018; Renbaum-Wolff et al., 2013) and also evolving
48 upon chemical aging and photochemistry (Baboomian et al., 2022). SOA phase state plays an
49 important role in a number of atmospheric multiphase processes (Shiraiwa et al., 2017). The
50 occurrence of glassy SOA in the free troposphere can impact activation pathways of ice crystals
51 and cloud droplets (Knopf and Alpert, 2023). Slow diffusion in viscous particles induces kinetic



52 limitations in heterogeneous and multiphase reactions (Zhang et al., 2018; Zhou et al., 2019;
53 Shiraiwa et al., 2011), affecting long-range transport (Shrivastava et al., 2017; Mu et al., 2018).
54 The timescale of SOA partitioning can be prolonged in viscous particles (Schervish and
55 Shiraiwa, 2023), retarding uptake of semi-volatile compounds and mixing of different particle
56 populations (Ye et al., 2016). Particle phase state also modulates SOA growth to cloud
57 condensation nuclei sizes, affecting cloud life cycle (Zaveri et al., 2022). While the phase states
58 of SOA generated by biogenic VOCs such as terpenes and isoprene have been extensively
59 studied (Virtanen et al., 2010; Petters et al., 2019; Renbaum-Wolff et al., 2013; Baboomian et
60 al., 2022; Zhang et al., 2018; Zhou et al., 2019), those derived from IVOCs are hardly
61 investigated and remain poorly constrained.

62 Viscosity (η) is a dynamic property that characterizes the particle phase state, which can
63 be derived from the glass transition temperature (T_g) of the constituting species (Koop et al.,
64 2011; Shiraiwa et al., 2011). Several structure-activity relationships models have been
65 developed to predict the T_g of an organic compound using various molecular properties
66 including molar mass, atomic O:C ratio (Shiraiwa et al., 2017), elemental composition (Derieux
67 et al., 2018), and volatility (Li et al., 2020; Zhang et al., 2019). These parameterizations do not
68 consider molecular structure nor functionality explicitly. Galeazzo and Shiraiwa (2022)
69 overcame this limitation by developing a machine learning-based model, tgBoost, with an
70 application of cheminformatics “molecular embeddings” that retains detailed information on
71 atomic composition, molecular structure and connectivity (Galeazzo and Shiraiwa, 2022). The
72 main novel feature introduced by tgBoost is model capability to predict different T_g for
73 structural isomers and high sensitivity of T_g to various functional groups, consistent with
74 viscosity measurements for functionalized compounds (Rothfuss and Petters, 2017; Grayson et
75 al., 2017).

76 Long-chain linear alkanes (n-alkanes) are representative IVOCs and account for a
77 substantial fraction of non-methane hydrocarbons in urban air as mainly emitted from
78 anthropogenic activities such as vehicle exhausts and incomplete fuel combustion (Li et al.,
79 2022). Gas-phase oxidation of n-alkanes by OH radicals can trigger the formation of SOA with
80 high yields, as observed in laboratory experiments (Aimanant and Ziemann, 2013a; Lim and
81 Ziemann, 2009b) and field observations (Gentner et al., 2012; Li et al., 2022). Gas-phase
82 oxidation pathways of n-alkanes are relatively well understood and successfully simulated by
83 detailed gas-phase chemistry modeling (Aumont et al., 2012; La et al., 2016), but the chemical
84 composition of n-alkane SOA has only been fully characterized for the C₁₆ n-alkane (Ranney
85 et al., 2023) and the phase state and viscosity of alkane SOA are unknown. Therefore, the n-



86 alkane SOA system provides an ideal benchmark for the investigation of the interplay of
87 chemical composition, particle phase state and kinetic limitations influencing SOA growth and
88 evolution.

89 In this study, we implemented tgBoost in an explicit gas-phase chemistry model
90 GECKO-A to investigate the complex interplay of chemical composition, kinetic partitioning,
91 and phase state of n-alkane SOA generated under dry and high NO_x conditions. The GECKO-
92 A model is to date one of the most comprehensive generators of gas-phase chemical schemes,
93 as it automatically generates detailed gas-phase chemical mechanisms involving thousands to
94 millions of oxidation products from a given VOC precursor based on established reaction
95 pathways and structure–activity relationships (Aumont et al., 2012; La et al., 2016). The
96 simulations were conducted with variable effective mass accommodation coefficient to
97 consider potential kinetic limitations in amorphous semisolid particles (Shiraiwa and Pöschl,
98 2021). The simulated results were compared with chamber experimental data on SOA yields
99 (Lim and Ziemann, 2009b) as well as new measurements on thermal desorption temperatures
100 and functional group distributions.

101

102 **Methods:**

103 **Model simulations.**

104 We applied the Generator for Explicit Chemistry and Kinetics of the Organics in the
105 Atmosphere (GECKO-A) (Aumont et al., 2012; La et al., 2016) to obtain detailed reaction
106 schemes of gas-phase OH oxidation of n-alkanes along with rate constants. The GECKO-A
107 generator used for oxidation of linear n-alkanes includes the latest structure-activity
108 relationships to treat the chemistry of organic compounds with OH radical (Jenkin et al., 2018a,
109 b; Jenkin et al., 2019), the bimolecular reactions of peroxy radicals (Jenkin et al., 2019), as well
110 as alkoxy radical decomposition and H migration reaction rates (Vereecken and Peeters, 2009;
111 La et al., 2016). The vapor pressures of semi-volatile species were estimated by using
112 Nannoolal’s group contribution method (Nannoolal et al., 2008) implemented in GECKO-A,
113 as described in detail in Valorso et al. (2011). Species with vapor pressure below 10⁻¹³ atm are
114 assumed to be of low enough volatility to completely partition to the condensed phase and their
115 gas phase chemistry is then not generated in the mechanism. The model treats unimolecular
116 particle-phase reactions including cyclization of hydroxyketones and dehydration of cyclic
117 hemiacetals to form dihydrofurans (La et al., 2016). The model does not treat autoxidation and
118 dimerization in the gas phase, but these processes should be minor pathways during n-alkane
119 oxidation in the presence of high NO_x as the reaction of peroxy radicals with NO_x should be



120 dominant (Praske et al., 2018; Pye et al., 2019); thus, their absence from GECKO-A chemical
121 schemes should not have major impacts on the simulated results.

122 These explicit chemical mechanisms were implemented into a box model to simulate
123 the multigenerational oxidation of n-alkanes, partitioning of oxidation products into the particle
124 phase based on their vapor pressures, and vapor wall loss to mimic chamber experiments (La
125 et al., 2016). We replicated the experimental conditions used in Lim and Ziemann (2009b) to
126 generate SOA from OH oxidation of C₈-C₁₇ n-alkanes at high NO_x conditions in the presence
127 of non-volatile dioctyl sebacate (DOS) seed particles with particle radius of 150 nm and mass
128 loading of 200 μg m⁻³. Temperature was held constant at 295.15 K, pressure was set at 1 atm
129 and RH was fixed at 0.5%. Photolysis frequencies were calculated based on the cross sections,
130 quantum yields as described in Aumont et al. (2005) and the photonic flux of blacklight lamps.
131 Each simulation ran for 1 hour and the time evolution of species concentration were computed
132 through a two-step method that solves stiff ordinary differential equations (Verwer, 1994;
133 Verwer et al., 1996). To investigate effects of mass concentrations, we also simulated
134 experiments of n-alkane photooxidation under high NO_x conditions with low mass loadings by
135 Presto et al. (2010). The number concentration of seed particles with particle diameter of 200
136 nm was ~5000 cm⁻³, corresponding to the mass concentration of ~20 μg m⁻³. Initial mixing
137 ratios of n-alkane and NO_x were in the range of 3 – 99 ppb and 1 – 5 ppm, respectively, as
138 reported in Presto et al. (2010) and these conditions were applied in the model.

139 The box model accounts for mass transfer kinetics of organic species between gas and
140 particle phases. Partitioning follows Raoult's law at equilibrium and partitioning kinetics is
141 described by the gas-particle mass transfer coefficient with the Fuchs-Sutugin approach
142 (Seinfeld and Pandis, 2016). For the base case scenario, we fixed the mass accommodation
143 coefficient (α) to be 1 based on molecular dynamics simulations (Julin et al., 2014), assuming
144 particles being low viscous liquids without kinetic limitations of bulk diffusion. To account for
145 potential kinetic limitations in viscous particles, we applied an effective mass accommodation
146 coefficient (α_{eff}) that is a function of volatility and bulk diffusivity (Shiraiwa and Pöschl, 2021):

$$147 \quad \alpha_{\text{eff}} = \alpha_s \frac{1}{1 + \frac{\alpha_s \omega C^0 r_p}{4 D_b \rho_p} \cdot 10^{-12} \frac{\text{g cm}^{-3}}{\mu\text{g m}^{-3}}} \quad (1)$$

148 where α_s is the surface accommodation coefficient assumed to be 1, ω (cm s⁻¹) is the mean
149 thermal velocity of the organic compound in the gas phase, r_p (cm) is the particle radius, ρ_p (g
150 cm⁻³) is the particle density, and C^0 (μg m⁻³) is the pure compound saturation mass
151 concentration. D_b (cm² s⁻¹) is bulk diffusivity as simulated by conversion of viscosity as detailed



152 below. α_{eff} values are shown as a function of D_b and vapor pressure p^o in Fig S3a. We
153 accounted for a reversible gas-to-chamber wall partitioning of gases and assumed a fixed first-
154 order deposition rate constant of $5 \times 10^{-4} \text{ s}^{-1}$ based on experimental observations and previous
155 modeling studies (Krechmer et al., 2016; La et al., 2016; Lim and Ziemann, 2009b). A
156 desorption rate constant from wall to the gas phase was derived by using a parameter of
157 $C_w/M_w\gamma_w$ of $9 \mu\text{mole m}^{-3}$ for n-alkanes and $120 \mu\text{mole m}^{-3}$ for oxidation products based on
158 chamber observations (Matsunaga and Ziemann, 2010), as discussed in La et al. (2016).

159 The glass transition temperatures (T_g) of organic compounds were predicted by the
160 machine learning-based model tgBoost (Galeazzo and Shiraiwa, 2022) and the
161 parameterization based on elemental composition (Derieux et al., 2018; Li et al., 2020). The
162 implementation of the compositional parametrization into the GECKO-A box model was done
163 in Galeazzo et al. (2021) with a thorough description of all the equations, assumptions and steps
164 adopted for the implementation of this viscosity estimation method. In this study we
165 implemented tgBoost, a newly developed machine learning model for better prediction of T_g .
166 tgBoost is a powerful model that can discern compositional isomers by functionality and predict
167 the glass transition temperature of an organic compound i ($T_{g,i}$) with an uncertainty of $\pm 18.3 \text{ K}$
168 using the canonical SMILES notation of a molecule (Galeazzo and Shiraiwa, 2022). We have
169 implemented a pipeline (i.e., gecko2vec) into GECKO-A to predict T_g of compounds from the
170 chemical mechanism in a fast and computationally efficient manner. Gecko2vec executes three
171 main steps: first, it translates the IDs of the compounds of interest of the GECKO-A mechanism
172 into the respective canonical SMILES notations (translation step); second, it transforms the
173 canonical SMILES notations into the respective molecular embeddings (i.e., unique 300-
174 dimensional numerical representations of molecules; embedding step); and finally, the
175 pretrained tgBoost model and its weights are loaded and used to predict T_g of each species
176 (prediction step). Within the box model, the T_g of total SOA particles ($T_{g,\text{org}}$) resulting from the
177 combination of its organic component and water mixture is computed using the Gordon–Taylor
178 equation (Dette et al., 2014; Koop et al., 2011; Zobrist et al., 2008). $T_{g,\text{org}}$ can be converted to
179 viscosity based on the Vogel-Tammann-Fulcher approach (Derieux et al., 2018) and viscosity
180 is further converted into bulk diffusivity using the fractional Stokes–Einstein equation (Evoy et
181 al., 2019).

182

183 **Laboratory experiments.**

184 SOA particles were generated from OH oxidation of C_8 – C_{17} n-alkanes in a 5.9 m^3 Teflon
185 environmental chamber filled with clean air under high NO_x conditions in the presence of non-



186 volatile dioctyl sebacate (DOS) seed particles, as described in detail elsewhere (Lim and
187 Ziemann, 2009b). Briefly, 1 ppm of n-alkane, 10 ppm of methyl nitrite, and 10 ppm of NO were
188 added to the chamber from a glass bulb, and $\sim 200\text{--}400 \mu\text{g m}^{-3}$ of seed particles were added
189 from an evaporation-condensation apparatus. Relatively high mass concentrations of seed
190 particles were used so that semi-volatile compounds would condense to particles, minimizing
191 vapor deposition to chamber walls (Zhang et al., 2014; Matsunaga and Ziemann, 2010).
192 Blacklights covering two of the chamber walls were then turned on for 60 min to form OH
193 radicals by methyl nitrite photolysis (Atkinson et al., 1981). The amount of n-alkane reacted
194 was measured by collecting Tenax samples before and after the experiment and analyzing by
195 gas chromatography with flame ionization detection (GC-FID). Aerosol volume concentrations
196 were measured using a scanning mobility particle sizer (Docherty et al., 2005) and converted
197 to an SOA mass formed using a density of 1.06 g cm^{-3} . SOA mass yields (mass of SOA
198 formed/mass of n-alkane reacted) were calculated from the measured SMPS mass (corrected
199 for particle wall loss using the $\sim 20\% \text{ h}^{-1}$ decay in mass after the lights were turned off) and the
200 GC-FID analyses. The SOA yields measured in these experiments were reported previously
201 (Lim and Ziemann, 2009b), but in light of a recent comparison of the accuracy of our SMPS
202 measurements with filter sampling the values reported here are higher by a factor of 1.24
203 (Bakker-Arkema and Ziemann, 2021). A temperature-programmed thermal desorption (TPTD)
204 method was also used to measure the composition and volatility of aerosol particles. Particles
205 were sampled directly from the chamber into a thermal desorption particle beam mass
206 spectrometer (Tobias et al., 2000), where they were formed into a beam inside an aerodynamic
207 lens, transported into a high vacuum chamber, and impacted on a copper rod vaporizer that was
208 coated with a non-stick polymer and cooled to -40°C . After sampling for 30 min, the vaporizer
209 was warmed by room air to -5°C and then heated at 2°C min^{-1} to 200°C . Compounds desorbed
210 according to volatility and entered a quadrupole mass spectrometer, where they were ionized
211 by 70 eV electrons prior to mass analysis. In one recent n-hexadecane experiment, we also
212 measured the composition of nitrate, hydroxyl, carbonyl (ketone + aldehyde), carboxylic acid,
213 ester, and peroxide functional groups in SOA using derivatization-spectrophotometric methods,
214 with the amount of $-\text{CH}_2-$ groups calculated by difference (Ranney et al., 2023). We note that
215 in that experiment the SOA yield measured by filter sampling was nearly identical to the one
216 we measured previously after applying the above correction.

217

218 **Results and discussion**

219 **SOA yields and viscosity.**



220 Figure 1(a) shows the measured yields of SOA generated from the oxidation of n-
221 alkanes (C_nH_{2n+2} ; $n = 8 - 17$) (Lim and Ziemann, 2009b). The model base case (black line) with
222 mass accommodation coefficient of 1 for all species represents no kinetic limitations in the
223 particle phase and the results are similar to previous simulations performed by La et al. (2016).
224 Vapor wall loss was considered based on experimental observations and previous modeling
225 studies (Krechmer et al., 2016; La et al., 2016; Lim and Ziemann, 2009b), which is important
226 to account for as no wall loss would lead to a significant overestimation of SOA yields, as
227 shown in the black dotted line and was discussed in detail in La et al. (2016). Both experimental
228 and simulated SOA yields increase with an increase of n , reflecting the decrease in volatility of
229 the precursor and its oxidation products (Shiraiwa et al., 2014). The observed SOA yield trend
230 is consistent with measurements by a thermal desorption particle beam mass spectrometer,
231 showing that n-alkane SOA are composed of less oxidized products with volatility lower for
232 precursors with higher n (Lim and Ziemann, 2009b, a).

233 The overall good agreement suggests that multigenerational chemistry in the gas phase
234 and partitioning of semi- and low-volatile products, as explicitly treated by GECKO-A box
235 modeling, are the dominant pathway of n-alkane SOA formation under these conditions. It also
236 suggests that peroxy radicals (RO_2) mainly react with NO_x , minimizing auto-oxidation and
237 gas-phase dimerization by $RO_2 + RO_2$ reactions. Good model agreement also suggests minor
238 contributions from particle-phase oligomerization chemistry, while particle-phase unimolecular
239 reactions including cyclization of hydroxyketones and dehydration of cyclic hemiacetals
240 forming dihydrofurans are treated in the model as they are important for the further oxidation
241 due to the presence of a double bond in the dihydrofurans (Lim and Ziemann, 2009a; La et al.,
242 2016). Thus, the GECKO-A model seemingly treats all essential processes for simulations of
243 n-alkane SOA formation under high NO_x conditions. Note that particle-phase chemistry was
244 shown to be substantial in n-alkane SOA formation under low NO_x conditions through
245 peroxyhemiacetal and oligomer formation (Shiraiwa et al., 2013; Ziemann and Atkinson, 2012).

246 To explore the potential impacts of particle phase state on SOA formation and
247 partitioning, we implemented effective mass accommodation coefficient (α_{eff}) that can
248 effectively consider kinetic limitations of bulk diffusion and also account for the effect of vapor
249 pressure on partitioning kinetics for species with various volatilities (Shiraiwa and Pöschl,
250 2021). Bulk diffusivity evolves upon SOA formation, which can be derived by viscosity and
251 glass transition temperature as predicted from the machine learning-based tgBoost model
252 (dashed green line) and the compositional parametrization (CP, dashed orange line). The
253 simulated SOA yields with tgBoost are very similar to the base case scenario with $\alpha = 1$, while



254 the application of the CP leads to smaller SOA yields for $n = 15-17$. These results indicate that
255 α_{eff} is close to 1 with little kinetic limitations of bulk diffusion for most cases, except some
256 limitations are predicted by CP for large precursors. Deviations of tgBoost and CP stem from
257 the difference in phase state and viscosity predicted by the two methods.

258 Figure 2(a) shows the simulated viscosity and corresponding bulk diffusivity of n-
259 alkane SOA. Remarkably, the two models predict contrasting trends. The simulated glass
260 transition temperature ($T_{\text{g,org}}$) of SOA is presented in Fig. A1. The CP predicts a decrease in
261 $T_{\text{g,org}}$ for C₈₋₁₂ with the lowest $T_{\text{g,org}}$ of ~ 250 K followed by an increase of $T_{\text{g,org}}$ with n to reach
262 ~ 270 K with C₁₇. These values correspond to viscosity of $10^4 - 10^6$ Pa s, indicating that n-alkane
263 SOA adopts viscous semisolid phase state. The increase of viscosity for larger precursors is
264 apparently reasonable, as their oxidation products would have higher molar mass which would
265 generally correspond to higher $T_{\text{g,org}}$ (Koop et al., 2011; Shiraiwa et al., 2017). Based on the
266 Stokes-Einstein relation, bulk diffusivity would be in the range of $3 \times 10^{-15} - 10^{-12}$ cm² s⁻¹. The
267 characteristic timescale of bulk diffusion in an average particle diameter of 300 nm can be as
268 low as ~ 2 hours (Shiraiwa et al., 2011), which is longer than experimental timescale of one
269 hour. These low diffusivities and long diffusion timescale can induce concentration gradients
270 in the particle bulk, reducing α_{eff} to cause significant kinetic limitations to retard SOA growth,
271 which is not consistent with the measured SOA yields.

272 Surprisingly, tgBoost predicts the opposite trend, predicting a monotonic decrease of
273 $T_{\text{g,org}}$ and viscosity with an increase of n , suggesting that SOA phase state shifts from an
274 amorphous semisolid state ($10^2 < \eta < 10^5$ Pa s) towards a liquid-like phase state ($\eta < 10^2$ Pa s).
275 These results are counter-intuitive as T_{g} values of n-alkanes increases with an increase of n ,
276 which can be reproduced with great precision by tgBoost (Galeazzo and Shiraiwa, 2022). The
277 determinants explaining this unexpected trend are chemical composition and molecular
278 structure of the oxidation products as discussed below. The characteristic timescale of bulk
279 diffusion is less than one second in a low viscous state and high bulk diffusivity (Shiraiwa et
280 al., 2011) and SOA particles are expected to be homogeneously well-mixed. Hence, α_{eff} remains
281 very close to 1 with little kinetic limitation of bulk diffusion.

282 Unfortunately, no direct viscosity measurements of n-alkane SOA generated under high
283 NO_x conditions are available to date, while there are two studies for n-alkane SOA generated
284 under NO_x-free conditions. Saukko et al. (2012) (Saukko et al., 2012) observed that n-
285 heptadecane (C₁₇H₃₆) SOA with low O:C ratio did not bounce from an impactor plate. It
286 indicates that these particles adopted a liquid-like state, as indicated by the violet shading in



287 Fig. 2(a), which is consistent with the tgBoost prediction. Shiraiwa et al. (2013) estimated bulk
288 diffusivity of n-dodecane ($C_{12}H_{26}$) SOA generated without NO_x to be $10^{-12} \text{ cm}^2 \text{ s}^{-1}$ using a
289 kinetic multilayer model to simulate evolution of particle size distribution. While these two data
290 points cannot be directly compared with the viscosity predictions of high NO_x n-alkane SOA,
291 they serve as reference data points for now and direct viscosity or bulk diffusivity
292 measurements of high NO_x n-alkane SOA are warranted in future studies.

293 Figure 2(b) shows the thermal desorption profiles of DOS that was present as seed
294 particles within the SOA formed from oxidation of the n-alkanes. Since DOS desorption
295 involved diffusion through the SOA prior to escape into vacuum, these profiles provided a
296 means for probing the SOA viscosity. The peaks in the DOS profiles for the C_{8-13} and C_{14-17} n-
297 alkanes are closely grouped, with vaporizer temperature at $\sim 80^\circ\text{C}$ and $\sim 65^\circ\text{C}$, respectively,
298 with the peak for pure DOS occurring in between at $\sim 72^\circ\text{C}$. The observed decrease in desorption
299 temperatures from low to high carbon numbers suggests an increase in effective volatility of
300 DOS in SOA generated from larger n-alkanes. In addition, Lim and Ziemann (2009) have
301 observed that C_{10} n-alkane SOA generated under high NO_x conditions evaporate at higher
302 temperatures compared to C_{12} and C_{15} n-alkane SOA based on total ion thermal desorption
303 measurements (Lim and Ziemann, 2009b). Volatility and T_g were shown to exhibit clear
304 anticorrelation (Li et al., 2020); hence, these results strongly indicate that C_{8-13} SOA have higher
305 T_g and viscosity compared to C_{13-17} SOA. It is remarkable to note that the C_{13} profile is bimodal
306 with peaks at $\sim 80^\circ\text{C}$ and $\sim 65^\circ\text{C}$ (Fig. 2b), which is in line with tgBoost prediction that the
307 viscosity of C_{13} alkane SOA is at the edge of amorphous semi-solid and liquid phase states (Fig.
308 2a). These results indicate that n-alkane SOA generated by larger precursors adopt low viscous
309 liquid-like states, while n-alkane SOA generated by smaller precursors adopt viscous semisolid
310 states, in agreement with tgBoost predictions. The major strength of tgBoost is that it considers
311 molecular structure and functionality for T_g predictions, while the compositional
312 parameterization does not account for this effect, leading to intuitive but erroneous predictions.

313

314 **Chemical composition of SOA.**

315 Figure 1 also shows the simulated (b) N:C and (c) O:C ratios of SOA with $\alpha = 1$ (black
316 line) and $\alpha = \alpha_{\text{eff}}$ with T_g determined with tgBoost (green line) or the compositional
317 parameterization (orange line). The N:C ratio is very similar among all simulations being ~ 0.2
318 for C_8 and decreasing progressively to ~ 0.03 with each addition of a carbon atom in the
319 precursor. O:C ratios were calculated in two different ways by treating a nitrate ($-ONO_2$) group



320 to contain either three (solid lines) or one (dashed lines) oxygen atoms. One oxygen atom is
321 also considered because O:C ratios reported from aerosol mass spectrometer measurements
322 generally treat a nitrate group the same as a hydroxyl group, since they have the same effect on
323 oxidation state (Farmer et al., 2010). Similar to the N:C ratio, there is a constant decrease in
324 O:C of SOA with increasing n , which is consistent with previous measurements for n -
325 pentadecane ($C_{15}H_{32}$) SOA (Aimanant and Ziemann, 2013a) and n -hexadecane ($C_{16}H_{34}$) SOA
326 in this study, even though the simulated values are ~45% and 15% lower than the measured
327 N:C and O:C ratios, respectively.

328 We measured functional group distributions in n -hexadecane SOA using derivatization-
329 spectrophotometric methods described in Aimanant and Ziemann (2013b), as shown in Fig.
330 1(d) and summarized in Table A1. Experimental measurements report high presence of $-CH_2-$
331 (13.81) and $-ONO_2$ (0.91), followed by ROH (0.41), RC(=O) (0.38), and RC(=O)OR (0.28),
332 with the average measured number of groups per C_{16} molecule in parenthesis. Figure 1(d)
333 includes simulation results by GECKO-A with CP and tgBoost, showing overall satisfactory
334 agreement. The simulated results with tgBoost show excellent agreement for hydroxyl and
335 methylene groups, while the simulated nitrates and carbonyls (ketones + aldehydes) are lower
336 than the measurements. The simulation by CP has also a similar trend, but with significantly
337 lower presence of nitrates, carbonyls, and esters.

338 Figure 3(a) shows the top 15 oxidation products in the particle phase formed by the
339 oxidation of n -hexadecane simulated by GECKO-A box model with tgBoost. Note that
340 positional isomers are lumped into one species and five species in the first row constitute
341 majority (~86%) of SOA mass. The simulated SOA is composed mostly by 1st generation
342 products including alkyl nitrates, hydroxynitrates, and hydroxyketones. There is also a
343 significant presence of 2nd and 3rd generation products such as esters and dinitrates. We also
344 found multi-functionalized decomposition products including smaller chain hydroxy nitrates
345 and alkyl lactones as well as particle-phase products from cyclization of hydroxyketones and
346 dehydration of cyclic hemiacetals to form dihydrofurans. There are notable differences in
347 molecular composition for SOA simulated by CP (Fig. A2): the major compounds are 1st
348 generation single and multi-functionalized products, followed by some 2nd and 3rd generation
349 products, without decomposition products in the top species.

350 The simulated T_g by both methods for each compound are listed in Fig. 3. Overall
351 tgBoost predicts T_g to be 157 – 221 K which are much lower compared to CP, especially with
352 significant differences for organic nitrates and multi-functionalized species. As tgBoost
353 considers the molecular structure, functional group and atomic interconnectivity of a molecule,



354 it should make better predictions for multi-functionalized compounds based on the presence of
355 different functional groups. CP is based on elemental composition and it predicts high T_g for
356 compounds with high molar mass, predicting same T_g for isomers. In addition, the CP for
357 CHON compounds was developed based on T_g values mainly estimated from their melting
358 points, as there are limited number of CHON compounds with measured T_g available. T_g of
359 organic nitrates are especially scarce and future T_g measurements for organic nitrates are desired
360 to improve T_g parameterizations. For these reasons, CP overestimates T_g for oxidation products
361 of n-alkane with long chain on average by ~66 K compared to tgBoost, overpredicting SOA
362 viscosity as shown in Fig. 2(a).

363 Figure 3 also lists α_{eff} values, showing that they are very close to 1 for tgBoost, with
364 SOA to be low viscous liquid with little kinetic limitations in mass accommodation. Additional
365 oxidation products with lower concentrations are listed in Fig. A3 and their α_{eff} remain also
366 close to 1. In contrast, as CP predicts SOA phase state to be viscous amorphous semisolid, α_{eff}
367 values for semi-volatile compounds become significantly smaller to kinetically limit mass
368 accommodation. This decrease of α_{eff} is larger for compounds with higher volatility, as such
369 compounds have higher re-evaporation rate on viscous particles with lower rate of bulk
370 diffusion (Shiraiwa and Pöschl, 2021) (Fig. A3). α_{eff} for lower volatility compounds remain
371 high, as they exhibit much lower desorption rates and are less likely to re-evaporate, even if
372 their diffusion into the bulk is slow. Consequently, SOA simulated with CP mainly consists of
373 later generation products with higher functionalization and molar masses.

374 Figure 3(b) shows top 15 oxidation products of n-decane ($\text{C}_{10}\text{H}_{26}$) as predicted by
375 GECKO-A with tgBoost. SOA is mostly composed of 2nd and 3rd generation products with
376 multiple functional groups including nitrates, ketones, and alcohols. These highly oxidized
377 products have T_g in the range of 225 – 304 K, with similar predictions by CP and tgBoost. This
378 is consistent with previous studies that demonstrated successful applications of CP to predict
379 the measured viscosity of SOA derived from biogenic and other relatively small precursors
380 (Derieux et al., 2018; Smith et al., 2021; Baboomian et al., 2022). These results are consistent
381 with total ion thermal desorption profiles of n-alkane SOA formed in the presence of NO_x (Lim
382 and Ziemann, 2009b): C_{10} SOA was observed to have a broad single peak around ~75 °C,
383 indicating the presence of low volatility multigenerational products; in contrast, C_{12} and C_{15}
384 SOA exhibited two peaks with one larger peak at lower temperature, corresponding to 1st
385 generation products and another smaller peak for multigenerational products. The phase state



386 of n-decane SOA is predicted to be semisolid, but kinetic limitations are not strong as α_{eff} values
387 for most compounds are only slightly reduced from 1.

388

389 **Effects of mass loadings on viscosity.**

390 The use of higher mass loadings in chamber experiments than ambient conditions
391 assured that the condensation of semi-volatile vapors to suspended particles is a dominant
392 process over vapor wall deposition (Zhang et al., 2014; Matsunaga and Ziemann, 2010).
393 Chamber experiments of n-alkane photooxidation at high NO_x were also conducted with lower
394 mass loading by Presto et al. (2010). As shown in Fig. 4(a), SOA yields are increased with an
395 increase of SOA mass concentrations, which is consistent with SOA absorptive partitioning
396 theory (Pankow, 1994). The oxidation of larger precursors leads to higher SOA yields, in
397 agreement with Lim and Ziemann (2009b) as presented in Fig. 1a. As shown with solid lines,
398 the GECKO-A box model simulated experimental observations very well.

399 Figure 4(b) depicts the simulated SOA viscosity. We observed the same trend as Fig.
400 2(a) with lowering of viscosity upon an increase of carbon number n . SOA phase state is
401 predicted to be semisolid for low carbon n , while it is expected to be liquid for high n . The
402 predicted viscosity is about one order of magnitude higher compared to Fig. 2(a). Lower mass
403 loadings suppress partitioning of higher volatility compounds, resulting in higher viscosity as
404 condensation would be dominated by lower volatility compounds with higher T_g (Jain et al.,
405 2018; Champion et al., 2019; Grayson et al., 2016; Derieux et al., 2018).

406

407 **Atmospheric Implications.**

408 The phase state and viscosity of SOA formed by IVOCs have been largely unknown
409 and unexplored. We demonstrated in this study that SOA derived from small and middle size
410 n-alkane (C_{12} and smaller) mostly consists of multigenerational oxidation products to adopt an
411 amorphous semisolid state, while larger n-alkane SOA are mainly composed of first generation
412 lightly oxidized products to adopt a low viscous liquid state. This result is surprising and
413 counterintuitive, as it has been established that higher molar mass would lead to higher glass
414 transition temperature, and hence, higher viscosity (Koop et al., 2011; Shiraiwa et al., 2017). In
415 fact, the viscosity of biogenic SOA follows this trend: the viscosity of isoprene (C_5H_8) SOA is
416 reported to be lower than monoterpene ($\text{C}_{10}\text{H}_{16}$, such as α -pinene and limonene) SOA
417 (Renbaum-Wolff et al., 2013; Zhang et al., 2019), while oxidation products of sesquiterpene
418 ($\text{C}_{15}\text{H}_{24}$) increase viscosity of SOA (Smith et al., 2021), which is captured by empirical
419 parameterizations based on elemental composition (Derieux et al., 2018; Li et al., 2020). In



420 contrast, n-alkane SOA exhibits an opposite trend, as indicated by thermal desorption
421 measurements that show that DOS in SOA formed by oxidation of large n-alkanes has higher
422 volatility. Hence, the SOA has lower viscosity, due to the enhanced presence of less
423 functionalized first-generation products (Li et al., 2020; Zhang et al., 2019). This trend is
424 successfully predicted by GECKO-A combined with machine learning-based model tgBoost,
425 which emphasizes the importance of consideration of functionality and molecular structure in
426 accurate predictions of T_g . The relationship between viscosity and composition is also reflected
427 in the atomic O:C and N:C ratios of n-alkane SOA, which decrease monotonically upon an
428 increase of carbon number of the n-alkane, since higher oxidation state and functionalization
429 can increase T_g (Derieux et al., 2018; Koop et al., 2011; Shiraiwa et al., 2017; Saukko et al.,
430 2012).

431 IVOCs gain growing attention for better characterization of urban air quality, as they
432 represent an important source of SOA as shown by chamber experiments (Aimanant and
433 Ziemann, 2013a; Lim and Ziemann, 2009b) and as observed in field observations (Gentner et
434 al., 2012; Li et al., 2022; Robinson et al., 2007; McDonald et al., 2018). While a few large-scale
435 aerosol models treat IVOC SOA to achieve better agreement with ambient measurements (De
436 Gouw et al., 2011; Li et al., 2022; Zhao et al., 2016), IVOC SOA is still highly uncertain in
437 terms of chemical composition and particle phase state and model parameters and treatments
438 for SOA formation and partitioning are poorly constrained. Our study provides critical insights
439 for these aspects, showing that n-alkane SOA formation under high NO_x conditions (as usually
440 the case for ambient urban air) is dominated by gas-phase chemistry followed by partitioning.
441 As the generated SOA particles adopt a low viscous state, there is little kinetic limitations of
442 mass accommodation and bulk diffusion, which supports the application of equilibrium SOA
443 partitioning in the boundary layer. While the experiments and modeling were conducted for dry
444 conditions in this study, the phase state and viscosity of ambient n-alkane SOA would be
445 expected to be even lower under humid conditions due to hygroscopic growth and water acting
446 as plasticizer. Note that further experiments and model simulations are required for different
447 conditions for middle and upper free troposphere, as viscosity is expected to become higher
448 under low temperatures.

449 It is highly remarkable that the combination of tgBoost and GECKO-A box model
450 accurately simulates SOA yields, functional group distributions and phase state. This new
451 model represents a unique and comprehensive tool for simulating formation, partitioning and
452 chemical evolution of SOA, opening up a new avenue for analyzing complex interplay of gas-
453 phase chemistry and particle-phase processes and composition in SOA for detailed analysis and



454 interpretation of laboratory experiments and field observations. In addition, we propose to
455 pursue the application of this model as a basis for the development of a detailed master
456 mechanism of multiphase aerosol chemistry as well as for the derivation of simplified but
457 realistic parameterizations for air quality and climate models. In regional and global air quality
458 models, it is challenging and computationally very expensive to treat complex SOA multiphase
459 processes. Thus, such processes should be treated in efficient but effective way and the new
460 model shall serve as benchmark for the development of simplified SOA descriptions.

461

462

463 **Acknowledgements.** This work was also funded by U.S. Department of Energy (DE-
464 SC0018349), U.S. National Science Foundation (AGS-1654104) and the Campus France
465 (Make Our Planet Great Again short stay program grant, mopga-short-000000116). In
466 addition, PZ acknowledges support from the National Science Foundation under grant AGS-
467 1750447.

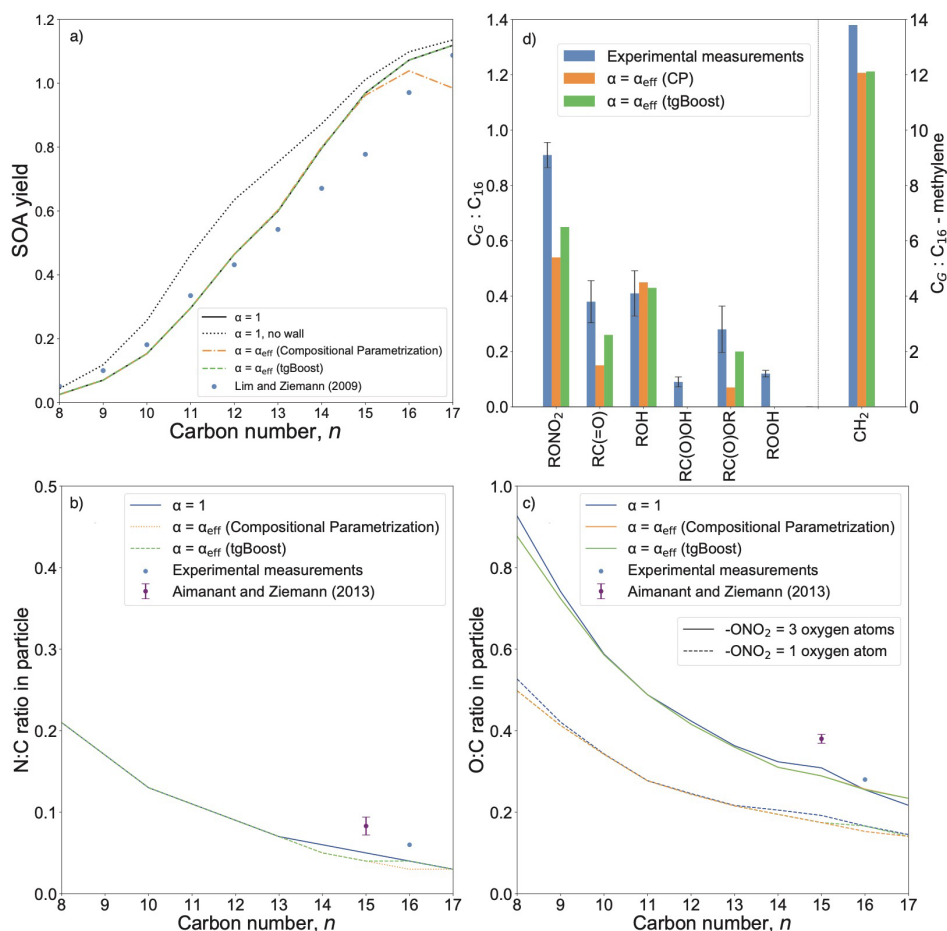
468

469 **Authors contributions.** TG and MS designed the study. TG conducted model simulations and
470 data analysis. RV, MC, and BA developed the GECKO-A model. YL and PZ conducted
471 experimental measurements. All authors discussed the results. TG and MS wrote the manuscript
472 with contributions from all coauthors.

473 **Competing interests.** At least one of the (co-)authors is a member of the editorial board of
474 Atmospheric Chemistry and Physics.

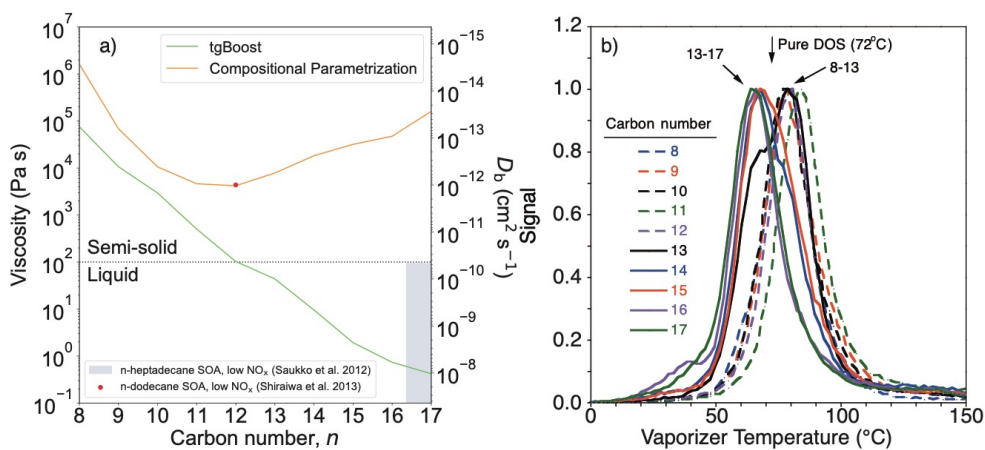
475 **Code/Data availability.** The simulation data may be obtained from the corresponding author
476 upon request. The model tgBoost is available in Github (<https://github.com/U0M0Z/tgpipe>) and
477 in the homepage (<https://azothai.ps.uci.edu/>).

478



479

480 **Figure 1:** (a) Yields of SOA generated from OH oxidation of linear n-alkanes as measured by
 481 Lim and Ziemann (2009) (markers) (Lim and Ziemann, 2009b) and modeled by the GECKO-
 482 A box model (lines). The black line represents the base case with mass accommodation
 483 coefficient (α) of 1. The dashed lines represent simulations with effective mass accommodation
 484 coefficient (α_{eff}) as a function of bulk diffusivity from tgBoost (green) and the compositional
 485 parameterization (orange). (b) N:C and (c) O:C ratios in SOA formed by n-alkane oxidation
 486 simulated by the GECKO-A box model. The black line represents the base case with α of 1.
 487 The dashed lines represent simulations with α_{eff} with tgBoost (green) and the compositional
 488 parameterization (orange). (d) Simulated functional group distributions of n-hexadecane
 489 ($\text{C}_{16}\text{H}_{34}$) oxidation products in the particle phase. The blue bars represent experimental
 490 measurements. The green and orange bars represent GECKO-A box model simulations with
 491 α_{eff} with tgBoost and the compositional parameterization, respectively.



492

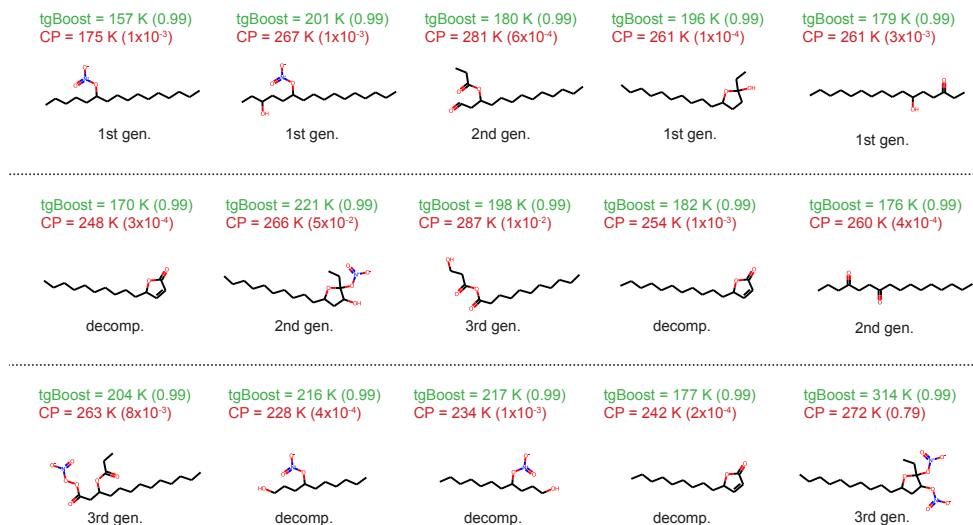
493 **Figure 2:** Phase state of n-alkane SOA. (a) Predicted viscosity of SOA generated from n-
494 alkanes as computed by the GECKO-A box model with the T_g compositional parametrization
495 (orange line) and tgBoost (green line) at the last step of the simulations ($t = 3600$ s). (b) Thermal
496 desorption temperatures of n-alkane SOA (C_{8-17}) formed on dioctyl sebacate (DOS) seed
497 particles under high NO_x conditions.

498

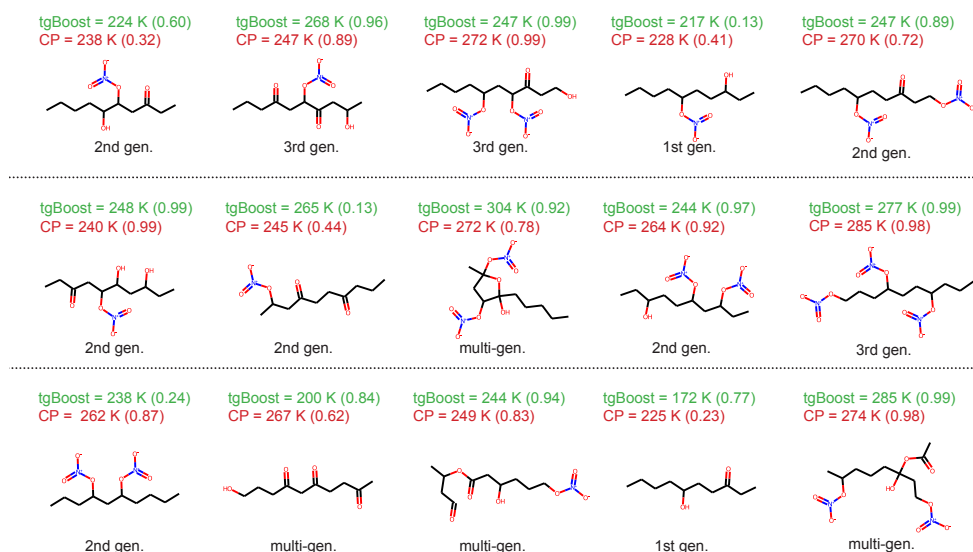
499



(a) n-Hexadecane (C₁₆)

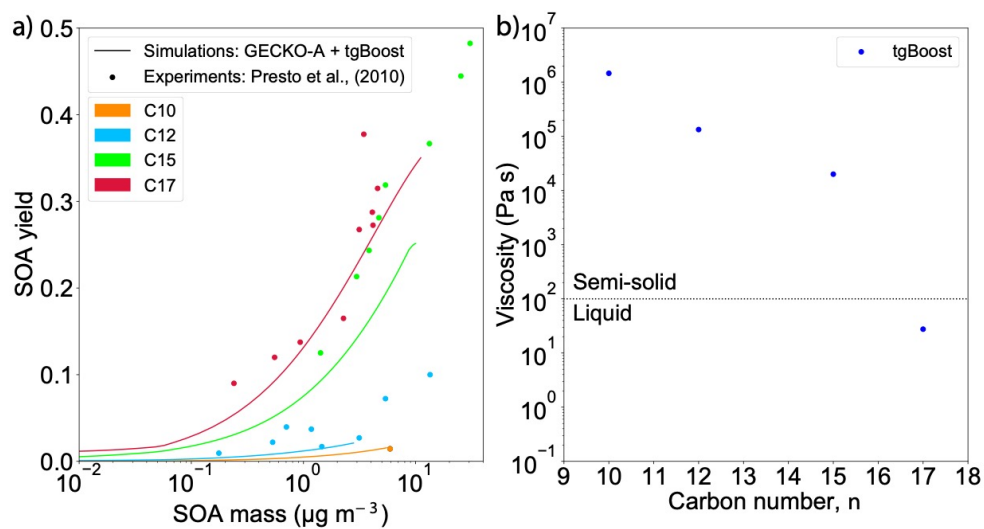


(b) n-Decane (C₁₀)



500
 501
 502
 503
 504
 505
 506
 507
 508

Figure 3: Molecular composition of oxidation products of n-alkanes under high NO_x conditions in the particle phase. Top 15 SOA contributors with highest concentrations in (a) n-Hexadecane (C₁₆H₃₄) SOA and (b) n-Decane (C₁₀H₂₂) simulated by GECKO-A with effective mass accommodation coefficient (α_{eff}) with tgBoost. The species are reported in descending concentrations from left to right and from top to bottom. Positional isomers are lumped into one species. Listed values are T_g as calculated by tgBoost and CP and α_{eff} values at the end of simulation (3600 s) in brackets. Types of compounds are also noted (1st, 2nd, and 3rd generation products, decomposition products).



509
510
511
512
513
514
515
516

Figure 4: Effects of mass loadings on SOA yields and viscosity. (a) SOA yields from photo-oxidation of n-decane (C10), n-dodecane (C12), n-pentadecane (C15), and n-heptadecane (C17) at high NO_x as a function of SOA mass concentration, as measured in Presto et al. (2010) (markers) and as modeled by the GECKO-A box model combined with tgBoost (lines). (b) SOA viscosity as modeled by the GECKO-A box model combined with tgBoost.



517 **References.**

- 518 Aimanant, S. and Ziemann, P. J.: Chemical Mechanisms of Aging of Aerosol Formed from the
519 Reaction of n-Pentadecane with OH Radicals in the Presence of NO_x, *Aerosol Sci. Technol.*,
520 47, 979-990, 10.1080/02786826.2013.804621, 2013a.
- 521 Aimanant, S. and Ziemann, P. J.: Development of Spectrophotometric Methods for the Analysis
522 of Functional Groups in Oxidized Organic Aerosol, *Aerosol Sci. Technol.*, 47, 581-591,
523 10.1080/02786826.2013.773579, 2013b.
- 524 Atkinson, R., Carter, W. P. L., Winer, A. M., and Pitts, J. N.: An Experimental Protocol for the
525 Determination of OH Radical Rate Constants with Organics Using Methyl Nitrite Photolysis
526 as an OH Radical Source, *Journal of the Air Pollution Control Association*, 31, 1090-1092,
527 10.1080/00022470.1981.10465331, 1981.
- 528 Aumont, B., Szopa, S., and Madronich, S.: Modelling the evolution of organic carbon during
529 its gas-phase tropospheric oxidation: development of an explicit model based on a self
530 generating approach, *Atmospheric Chemistry and Physics*, 5, 2497-2517, 10.5194/acp-5-2497-
531 2005, 2005.
- 532 Aumont, B., Valorso, R., Mouchel-Vallon, C., Camredon, M., Lee-Taylor, J., and Madronich,
533 S.: Modeling SOA formation from the oxidation of intermediate volatility n-alkanes,
534 *Atmospheric Chemistry and Physics*, 12, 7577-7589, 10.5194/acp-12-7577-2012, 2012.
- 535 Baboosian, V. J., Crescenzo, G. V., Huang, Y., Mahrt, F., Shiraiwa, M., Bertram, A. K., and
536 Nizkorodov, S. A.: Sunlight can convert atmospheric aerosols into a glassy solid state and
537 modify their environmental impacts, *Proc. Nat. Acad. Sci.*, 119, e2208121119,
538 10.1073/pnas.2208121119, 2022.
- 539 Bakker-Arkema, J. G. and Ziemann, P. J.: Minimizing Errors in Measured Yields of Particle-
540 Phase Products Formed in Environmental Chamber Reactions: Revisiting the Yields of β -
541 Hydroxynitrates Formed from 1-Alkene + OH/NO_x Reactions, *ACS Earth and Space*
542 *Chemistry*, 5, 690-702, 10.1021/acsearthspacechem.1c00008, 2021.
- 543 Champion, W. M., Rothfuss, N. E., Petters, M. D., and Grieshop, A. P.: Volatility and Viscosity
544 Are Correlated in Terpene Secondary Organic Aerosol Formed in a Flow Reactor,
545 *Environmental Science & Technology Letters*, 6, 513-519, 10.1021/acs.estlett.9b00412, 2019.
- 546 de Gouw, J. A., Middlebrook, A. M., Warneke, C., Ahmadov, R., Atlas, E. L., Bahreini, R.,
547 Blake, D. R., Brock, C. A., Brioude, J., Fahey, D. W., Fehsenfeld, F. C., Holloway, J. S., Le
548 Henaff, M., Lueb, R. A., McKeen, S. A., Meagher, J. F., Murphy, D. M., Paris, C., Parrish, D.
549 D., Perring, A. E., Pollack, I. B., Ravishankara, A. R., Robinson, A. L., Ryerson, T. B.,
550 Schwarz, J. P., Spackman, J. R., Srinivasan, A., and Watts, L. A.: Organic Aerosol Formation
551 Downwind from the Deepwater Horizon Oil Spill, *Science*, 331, 1295-1299,
552 10.1126/science.1200320, 2011.
- 553 DeRieux, W. S. W., Li, Y., Lin, P., Laskin, J., Laskin, A., Bertram, A. K., Nizkorodov, S. A.,
554 and Shiraiwa, M.: Predicting the glass transition temperature and viscosity of secondary organic
555 material using molecular composition, *Atmos. Chem. Phys.*, 18, 6331-6351, 10.5194/acp-18-
556 6331-2018, 2018.



- 557 Dette, H. P., Qi, M., Schröder, D. C., Godt, A., and Koop, T.: Glass-forming properties of 3-
558 Methylbutane-1,2,3-tricarboxylic acid and its mixtures with water and pinonic acid, *The*
559 *Journal of Physical Chemistry A*, 118, 7024-7033, 10.1021/jp505910w, 2014.
- 560 Docherty, K. S., Wu, W., Lim, Y. B., and Ziemann, P. J.: Contributions of organic peroxides
561 to secondary aerosol formed from reactions of monoterpenes with O₃, *Environ. Sci. Technol.*,
562 39, 4049-4059, 10.1021/es050228s, 2005.
- 563 Evoy, E., Maclean, A. M., Rovelli, G., Li, Y., Tsimpidi, A. P., Karydis, V. A., Kamal, S.,
564 Lelieveld, J., Shiraiwa, M., Reid, J. P., and Bertram, A. K.: Predictions of diffusion rates of
565 large organic molecules in secondary organic aerosols using the Stokes–Einstein and fractional
566 Stokes–Einstein relations, *Atmos. Chem. Phys.*, 19, 10073-10085, 10.5194/acp-19-10073-
567 2019, 2019.
- 568 Farmer, D. K., Matsunaga, A., Docherty, K. S., Surratt, J. D., Seinfeld, J. H., Ziemann, P. J.,
569 and Jimenez, J. L.: Response of an aerosol mass spectrometer to organonitrates and
570 organosulfates and implications for atmospheric chemistry, *Proc. Nat. Acad. Sci.*, 107, 6670-
571 6675, 2010.
- 572 Galeazzo, T. and Shiraiwa, M.: Predicting glass transition temperature and melting point of
573 organic compounds via machine learning and molecular embeddings, *Environmental Science:*
574 *Atmospheres*, 2, 362-374, 10.1039/D1EA00090J, 2022.
- 575 Galeazzo, T., Valorso, R., Li, Y., Camredon, M., Aumont, B., and Shiraiwa, M.: Estimation of
576 secondary organic aerosol viscosity from explicit modeling of gas-phase oxidation of isoprene
577 and α -pinene, *Atmos. Chem. Phys.*, 21, 10199-10213, 10.5194/acp-21-10199-2021, 2021.
- 578 Gentner, D. R., Isaacman, G., Worton, D. R., Chan, A. W. H., Dallmann, T. R., Davis, L., Liu,
579 S., Day, D. A., Russell, L. M., Wilson, K. R., Weber, R., Guha, A., Harley, R. A., and Goldstein,
580 A. H.: Elucidating secondary organic aerosol from diesel and gasoline vehicles through detailed
581 characterization of organic carbon emissions, *Proc. Nat. Acad. Sci.*, 109, 18318-18323,
582 10.1073/pnas.1212272109, 2012.
- 583 Grayson, J. W., Zhang, Y., Mutzel, A., Renbaum-Wolff, L., Böge, O., Kamal, S., Herrmann,
584 H., Martin, S. T., and Bertram, A. K.: Effect of varying experimental conditions on the viscosity
585 of α -pinene derived secondary organic material, *Atmos. Chem. Phys.*, 16, 6027-6040,
586 10.5194/acp-16-6027-2016, 2016.
- 587 Grayson, J. W., Evoy, E., Song, M., Chu, Y., Maclean, A., Nguyen, A., Upshur, M. A.,
588 Ebrahimi, M., Chan, C. K., Geiger, F. M., Thomson, R. J., and Bertram, A. K.: The effect of
589 hydroxyl functional groups and molar mass on the viscosity of non-crystalline organic and
590 organic–water particles, *Atmos. Chem. Phys.*, 17, 8509-8524, 10.5194/acp-17-8509-2017,
591 2017.
- 592 Jain, S., Fischer, B. K., and Petrucci, A. G.: The Influence of Absolute Mass Loading of
593 Secondary Organic Aerosols on Their Phase State, *Atmosphere*, 9, 10.3390/atmos9040131,
594 2018.
- 595 Jenkin, M. E., Valorso, R., Aumont, B., and Rickard, A. R.: Estimation of rate coefficients and
596 branching ratios for reactions of organic peroxy radicals for use in automated mechanism
597 construction, *Atmos. Chem. Phys.*, 19, 7691-7717, 10.5194/acp-19-7691-2019, 2019.



- 598 Jenkin, M. E., Valorso, R., Aumont, B., Rickard, A. R., and Wallington, T. J.: Estimation of
599 rate coefficients and branching ratios for gas-phase reactions of OH with aromatic organic
600 compounds for use in automated mechanism construction, *Atmos. Chem. Phys.*, 18, 9329-9349,
601 10.5194/acp-18-9329-2018, 2018a.
- 602 Jenkin, M. E., Valorso, R., Aumont, B., Rickard, A. R., and Wallington, T. J.: Estimation of
603 rate coefficients and branching ratios for gas-phase reactions of OH with aliphatic organic
604 compounds for use in automated mechanism construction, *Atmos. Chem. Phys.*, 18, 9297-9328,
605 10.5194/acp-18-9297-2018, 2018b.
- 606 Jimenez, J. L., Canagaratna, M. R., Donahue, N. M., Prevot, A. S. H., Zhang, Q., Kroll, J. H.,
607 DeCarlo, P. F., Allan, J. D., Coe, H., Ng, N. L., Aiken, A. C., Docherty, K. S., Ulbrich, I. M.,
608 Grieshop, A. P., Robinson, A. L., Duplissy, J., Smith, J. D., Wilson, K. R., Lanz, V. A., Hueglin,
609 C., Sun, Y. L., Tian, J., Laaksonen, A., Raatikainen, T., Rautiainen, J., Vaattovaara, P., Ehn,
610 M., Kulmala, M., Tomlinson, J. M., Collins, D. R., Cubison, M. J., Dunlea, E. J., Huffman, J.
611 A., Onasch, T. B., Alfarra, M. R., Williams, P. I., Bower, K., Kondo, Y., Schneider, J.,
612 Drewnick, F., Borrmann, S., Weimer, S., Demerjian, K., Salcedo, D., Cottrell, L., Griffin, R.,
613 Takami, A., Miyoshi, T., Hatakeyama, S., Shimonono, A., Sun, J. Y., Zhang, Y. M., Dzepina, K.,
614 Kimmel, J. R., Sueper, D., Jayne, J. T., Herndon, S. C., Trimborn, A. M., Williams, L. R.,
615 Wood, E. C., Middlebrook, A. M., Kolb, C. E., Baltensperger, U., and Worsnop, D. R.:
616 Evolution of organic aerosols in the atmosphere, *Science*, 326, 1525-1529,
617 10.1126/science.1180353, 2009.
- 618 Julin, J., Winkler, P. M., Donahue, N. M., Wagner, P. E., and Riipinen, I. A.: Near unity mass
619 accommodation coefficient of organic molecules of varying structure, *Environ. Sci. Technol.*,
620 48, 12083–12089, 10.1021/es501816h, 2014.
- 621 Knopf, D. A. and Alpert, P. A.: Atmospheric ice nucleation, *Nat. Rev. Phys.*, 5, 203-217,
622 10.1038/s42254-023-00570-7, 2023.
- 623 Koop, T., Bookhold, J., Shiraiwa, M., and Pöschl, U.: Glass transition and phase state of organic
624 compounds: dependency on molecular properties and implications for secondary organic
625 aerosols in the atmosphere, *Physical Chemistry Chemical Physics*, 13, 19238-19255, 2011.
- 626 Krechmer, J. E., Pagonis, D., Ziemann, P. J., and Jimenez, J. L.: Quantification of gas-wall
627 partitioning in Teflon environmental chambers using rapid bursts of low-volatility oxidized
628 species generated in situ, *Environ. Sci. Technol.*, 50, 5757-5765, 2016.
- 629 Kroll, J. H. and Seinfeld, J. H.: Chemistry of secondary organic aerosol: Formation and
630 evolution of low-volatility organics in the atmosphere, *Atmos. Environ.*, 42, 3593-3624,
631 10.1016/j.atmosenv.2008.01.003, 2008.
- 632 La, Y. S., Camredon, M., Ziemann, P. J., Valorso, R., Matsunaga, A., Lannuque, V., Lee-
633 Taylor, J., Hodzic, A., Madronich, S., and Aumont, B.: Impact of chamber wall loss of gaseous
634 organic compounds on secondary organic aerosol formation: explicit modeling of SOA
635 formation from alkane and alkene oxidation, *Atmospheric Chemistry and Physics*, 16, 1417-
636 1431, 10.5194/acp-16-1417-2016, 2016.
- 637 Li, J. L., Li, K., Li, H., Wang, X. Z., Wang, W. G., Wang, K., and Ge, M. F.: Long-chain
638 alkanes in the atmosphere: A review *, *J. Environ. Sci.*, 114, 37-52, 10.1016/j.jes.2021.07.021,
639 2022.



- 640 Li, Y., Day, D. A., Stark, H., Jimenez, J. L., and Shiraiwa, M.: Predictions of the glass transition
641 temperature and viscosity of organic aerosols from volatility distributions, *Atmos. Chem. Phys.*,
642 20, 8103-8122, 10.5194/acp-20-8103-2020, 2020.
- 643 Lim, Y. B. and Ziemann, P. J.: Chemistry of Secondary Organic Aerosol Formation from OH
644 Radical-Initiated Reactions of Linear, Branched, and Cyclic Alkanes in the Presence of NO_x,
645 *Aerosol Sci. Technol.*, 43, 604-619, 10.1080/02786820902802567, 2009a.
- 646 Lim, Y. B. and Ziemann, P. J.: Effects of Molecular Structure on Aerosol Yields from OH
647 Radical-Initiated Reactions of Linear, Branched, and Cyclic Alkanes in the Presence of NO_x,
648 *Environ. Sci. Technol.*, 43, 2328-2334, 10.1021/es803389s, 2009b.
- 649 Matsunaga, A. and Ziemann, P. J.: Gas-wall partitioning of organic compounds in a Teflon film
650 chamber and potential effects on reaction product and aerosol yield measurements, *Aerosol Sci.*
651 *Technol.*, 44, 881-892, 10.1080/02786826.2010.501044, 2010.
- 652 McDonald, B. C., de Gouw, J. A., Gilman, J. B., Jathar, S. H., Akherati, A., Cappa, C. D.,
653 Jimenez, J. L., Lee-Taylor, J., Hayes, P. L., McKeen, S. A., Cui, Y. Y., Kim, S.-W., Gentner,
654 D. R., Isaacman-VanWertz, G., Goldstein, A. H., Harley, R. A., Frost, G. J., Roberts, J. M.,
655 Ryerson, T. B., and Trainer, M.: Volatile chemical products emerging as largest petrochemical
656 source of urban organic emissions, *Science*, 359, 760, 2018.
- 657 Mu, Q., Shiraiwa, M., Octaviani, M., Ma, N., Ding, A., Su, H., Lammel, G., Pöschl, U., and
658 Cheng, Y.: Temperature effect on phase state and reactivity controls atmospheric multiphase
659 chemistry and transport of PAHs, *Science Advances*, 4, eaap7314, 2018.
- 660 Nannoolal, Y., Rarey, J., and Ramjugernath, D.: Estimation of pure component properties - Part
661 3. Estimation of the vapor pressure of non-electrolyte organic compounds via group
662 contributions and group interactions, *Fluid Phase Equilibria*, 269, 117-133,
663 10.1016/j.fluid.2008.04.020, 2008.
- 664 Pankow, J. F.: An absorption-model of the gas aerosol partitioning involved in the formation
665 of secondary organic aerosol, *Atmos. Environ.*, 28, 189-193, 1994.
- 666 Petters, S. S., Kreidenweis, S. M., Grieshop, A. P., Ziemann, P. J., and Petters, M. D.:
667 Temperature- and Humidity-Dependent Phase States of Secondary Organic Aerosols,
668 *Geophysical Research Letters*, 46, 1005-1013, 10.1029/2018GL080563, 2019.
- 669 Pöschl, U. and Shiraiwa, M.: Multiphase Chemistry at the Atmosphere–Biosphere Interface
670 Influencing Climate and Public Health in the Anthropocene, *Chemical Reviews*, 115, 4440–
671 4475, 10.1021/cr500487s, 2015.
- 672 Praske, E., Otkjær, R. V., Crouse, J. D., Hethcox, J. C., Stoltz, B. M., Kjaergaard, H. G., and
673 Wennberg, P. O.: Atmospheric autoxidation is increasingly important in urban and suburban
674 North America, *Proc. Nat. Acad. Sci.*, 115, 64-69, 10.1073/pnas.1715540115, 2018.
- 675 Presto, A. A., Miracolo, M. A., Donahue, N. M., and Robinson, A. L.: Secondary organic
676 aerosol formation from high-NO_x photo-oxidation of low volatility precursors: n-alkanes,
677 *Environ. Sci. Technol.*, 44, 2029-2034, 10.1021/es903712r, 2010.
- 678 Pye, H. O. T., D'Ambro, E. L., Lee, B. H., Schobesberger, S., Takeuchi, M., Zhao, Y., Lopez-
679 Hilfiker, F., Liu, J., Shilling, J. E., Xing, J., Mathur, R., Middlebrook, A. M., Liao, J., Welti,



- 680 A., Graus, M., Warneke, C., de Gouw, J. A., Holloway, J. S., Ryerson, T. B., Pollack, I. B., and
681 Thornton, J. A.: Anthropogenic enhancements to production of highly oxygenated molecules
682 from autoxidation, *Proc. Nat. Acad. Sci.*, 116, 6641, 10.1073/pnas.1810774116, 2019.
- 683 Ranney, A. P., Longnecker, E. R., Ziola, A. C., and Ziemann, P. J.: Measured and Modeled
684 Secondary Organic Aerosol Products and Yields from the Reaction of n-Hexadecane +
685 OH/NO_x, *ACS Earth and Space Chemistry*, 7, 2298-2310,
686 10.1021/acsearthspacechem.3c00227, 2023.
- 687 Reid, J. P., Bertram, A. K., Topping, D. O., Laskin, A., Martin, S. T., Petters, M. D., Pope, F.
688 D., and Rovelli, G.: The viscosity of atmospherically relevant organic particles, *Nature*
689 *Communications*, 9, 956, 10.1038/s41467-018-03027-z, 2018.
- 690 Renbaum-Wolff, L., Grayson, J. W., Bateman, A. P., Kuwata, K., Sellier, M., Murray, B. J.,
691 Schilling, J. E., Martin, S. T., and Bertram, A. K.: Viscosity of α -pinene secondary organic
692 material and implications for particle growth and reactivity, *Proceedings of the National*
693 *Academy of Sciences of the United States of America*, 110, 8014-8019,
694 10.1073/pnas.1219548110 2013.
- 695 Robinson, A. L., Donahue, N. M., Shrivastava, M. K., Weitkamp, E. A., Sage, A. M., Grieshop,
696 A. P., Lane, T. E., Pierce, J. R., and Pandis, S. N.: Rethinking organic aerosols: Semivolatile
697 emissions and photochemical aging, *Science*, 315, 1259-1262, 10.1126/science.1133061, 2007.
- 698 Rothfuss, N. E. and Petters, M. D.: Influence of Functional Groups on the Viscosity of Organic
699 Aerosol, *Environ. Sci. Technol.*, 51, 271-279, 10.1021/acs.est.6b04478, 2017.
- 700 Saukko, E., Lambe, A. T., Massoli, P., Koop, T., Wright, J. P., Croasdale, D. R., Pedernera, D.
701 A., Onasch, T. B., Laaksonen, A., Davidovits, P., Worsnop, D. R., and Virtanen, A.: Humidity-
702 dependent phase state of SOA particles from biogenic and anthropogenic precursors,
703 *Atmospheric Chemistry and Physics*, 12, 7517-7529, 10.5194/acp-12-7517-2012, 2012.
- 704 Schervish, M. and Shiraiwa, M.: Impact of phase state and non-ideal mixing on equilibration
705 timescales of secondary organic aerosol partitioning, *Atmos. Chem. Phys.*, 23, 221-233,
706 10.5194/acp-23-221-2023, 2023.
- 707 Seinfeld, J. H. and Pandis, S. N.: *Atmospheric chemistry and physics: from air pollution to*
708 *climate change*, John Wiley & Sons 2016.
- 709 Shiraiwa, M. and Pöschl, U.: Mass accommodation and gas-particle partitioning in secondary
710 organic aerosols: dependence on diffusivity, volatility, particle-phase reactions, and penetration
711 depth, *Atmos. Chem. Phys.*, 21, 1565-1580, 10.5194/acp-21-1565-2021, 2021.
- 712 Shiraiwa, M., Ammann, M., Koop, T., and Pöschl, U.: Gas uptake and chemical aging of
713 semisolid organic aerosol particles, *Proc. Nat. Acad. Sci.*, 108, 11003-11008,
714 10.1073/pnas.1103045108, 2011.
- 715 Shiraiwa, M., Berkemeier, T., Schilling-Fahnestock, K. A., Seinfeld, J. H., and Pöschl, U.:
716 Molecular corridors and kinetic regimes in the multiphase chemical evolution of secondary
717 organic aerosol, *Atmos. Chem. Phys.*, 14, 8323-8341, 10.5194/acp-14-8323-2014, 2014.
- 718 Shiraiwa, M., Yee, L. D., Schilling, K. A., Loza, C. L., Craven, J. S., Zuend, A., Ziemann, P.
719 J., and Seinfeld, J. H.: Size distribution dynamics reveal particle-phase chemistry in organic



- 720 aerosol formation, *Proceedings of the National Academy of Sciences of the United States of*
721 *America*, 110, 11746-11750, 10.1073/pnas.1307501110, 2013.
- 722 Shiraiwa, M., Li, Y., Tsimpidi, A. P., Karydis, V. A., Berkemeier, T., Pandis, S. N., Lelieveld,
723 J., Koop, T., and Pöschl, U.: Global distribution of particle phase state in atmospheric secondary
724 organic aerosols, *Nature Communications*, 8, 15002, 10.1038/ncomms15002, 2017.
- 725 Shrivastava, M., Lou, S., Zelenyuk, A., Easter, R. C., Corley, R. A., Thrall, B. D., Rasch, P. J.,
726 Fast, J. D., Massey Simonich, S. L., Shen, H., and Tao, S.: Global long-range transport and lung
727 cancer risk from polycyclic aromatic hydrocarbons shielded by coatings of organic aerosol,
728 *Proc. Nat. Acad. Sci.*, 114, 1246-1251, 2017.
- 729 Smith, N. R., Crescenzo, G. V., Huang, Y., Hettiyadura, A. P. S., Siemens, K., Li, Y., Faiola,
730 C. L., Laskin, A., Shiraiwa, M., Bertram, A. K., and Nizkorodov, S. A.: Viscosity and liquid–
731 liquid phase separation in healthy and stressed plant SOA, *Environmental Science:*
732 *Atmospheres*, 1, 140-153, 10.1039/D0EA00020E, 2021.
- 733 Tobias, H. J., Kooiman, P. M., Docherty, K. S., and Ziemann, P. J.: Real-Time Chemical
734 Analysis of Organic Aerosols Using a Thermal Desorption Particle Beam Mass Spectrometer,
735 *Aerosol Sci. Technol.*, 33, 170-190, 10.1080/027868200410912, 2000.
- 736 Valorso, R., Aumont, B., Camredon, M., Raventos-Duran, T., Mouchel-Vallon, C., Ng, N. L.,
737 Seinfeld, J. H., Lee-Taylor, J., and Madronich, S.: Explicit modelling of SOA formation from
738 α -pinene photooxidation: sensitivity to vapour pressure estimation, *Atmospheric Chemistry and*
739 *Physics*, 11, 6895-6910, 10.5194/acp-11-6895-2011, 2011.
- 740 Vereecken, L. and Peeters, J.: Decomposition of substituted alkoxy radicals—part I: a
741 generalized structure–activity relationship for reaction barrier heights, *Physical Chemistry*
742 *Chemical Physics*, 11, 9062-9074, 2009.
- 743 Verwer, J. G.: Gauss–Seidel iteration for stiff ODEs from chemical kinetics, *SIAM Journal on*
744 *Scientific Computing*, 15, 1243-1250, 1994.
- 745 Verwer, J. G., Blom, J. G., and Hundsdorfer, W.: An implicit-explicit approach for atmospheric
746 transport-chemistry problems, *Applied Numerical Mathematics*, 20, 191-209, 1996.
- 747 Virtanen, A., Joutsensaari, J., Koop, T., Kannosto, J., YliPirilä, P., Leskinen, J., Mäkelä, J. M.,
748 Holopainen, J. K., Pöschl, U., Kulmala, M., Worsnop, D. R., and Laaksonen, A.: An amorphous
749 solid state of biogenic secondary organic aerosol particles, *Nature*, 467, 824-827,
750 doi:10.1038/nature09455, 2010.
- 751 Ye, Q., Robinson, E. S., Ding, X., Ye, P., Sullivan, R. C., and Donahue, N. M.: Mixing of
752 secondary organic aerosols versus relative humidity, *Proc. Nat. Acad. Sci.*, 113, 12649-12654,
753 2016.
- 754 Zaveri, R. A., Wang, J., Fan, J., Zhang, Y., Shilling John, E., Zelenyuk, A., Mei, F., Newsom,
755 R., Pekour, M., Tomlinson, J., Comstock Jennifer, M., Shrivastava, M., Fortner, E., Machado
756 Luiz, A. T., Artaxo, P., and Martin Scot, T.: Rapid growth of anthropogenic organic
757 nanoparticles greatly alters cloud life cycle in the Amazon rainforest, *Science Advances*, 8,
758 eabj0329, 10.1126/sciadv.abj0329, 2022.



- 759 Zhang, X., Cappa, C. D., Jathar, S. H., McVay, R. C., Ensberg, J. J., Kleeman, M. J., and
760 Seinfeld, J. H.: Influence of vapor wall loss in laboratory chambers on yields of secondary
761 organic aerosol, *Proc. Nat. Acad. Sci.*, 111, 5802-5807, 2014.
- 762 Zhang, Y., Chen, Y., Lambe, A. T., Olson, N. E., Lei, Z., Craig, R. L., Zhang, Z., Gold, A.,
763 Onasch, T. B., Jayne, J. T., Worsnop, D. R., Gaston, C. J., Thornton, J. A., Vizuete, W., Ault,
764 A. P., and Surratt, J. D.: Effect of the Aerosol-Phase State on Secondary Organic Aerosol
765 Formation from the Reactive Uptake of Isoprene-Derived Epoxydiols (IEPOX), *Environmental
766 Science & Technology Letters*, 5, 167-174, 10.1021/acs.estlett.8b00044, 2018.
- 767 Zhang, Y., Nichman, L., Spencer, P., Jung, J. I., Lee, A., Heffernan, B. K., Gold, A., Zhang, Z.,
768 Chen, Y., Canagaratna, M. R., Jayne, J. T., Worsnop, D. R., Onasch, T. B., Surratt, J. D.,
769 Chandler, D., Davidovits, P., and Kolb, C. E.: The Cooling Rate- and Volatility-Dependent
770 Glass-Forming Properties of Organic Aerosols Measured by Broadband Dielectric
771 Spectroscopy, *Environ. Sci. Technol.*, 53, 12366-12378, 10.1021/acs.est.9b03317, 2019.
- 772 Zhao, B., Wang, S., Donahue, N. M., Jathar, S. H., Huang, X., Wu, W., Hao, J., and Robinson,
773 A. L.: Quantifying the effect of organic aerosol aging and intermediate-volatility emissions on
774 regional-scale aerosol pollution in China, *Sci. Rep.*, 6, 28815, 10.1038/srep28815, 2016.
- 775 Zhou, S., Hwang, B. C. H., Lakey, P. S. J., Zuend, A., Abbatt, J. P. D., and Shiraiwa, M.:
776 Multiphase reactivity of polycyclic aromatic hydrocarbons is driven by phase separation and
777 diffusion limitations, *Proc. Nat. Acad. Sci.*, 116, 11658-11663, 10.1073/pnas.1902517116,
778 2019.
- 779 Ziemann, P. J. and Atkinson, R.: Kinetics, products, and mechanisms of secondary organic
780 aerosol formation, *Chemical Society Reviews*, 41, 6582-6605, 2012.
- 781 Zobrist, B., Marcolli, C., Pedernera, D. A., and Koop, T.: Do atmospheric aerosols form
782 glasses?, *Atmospheric Chemistry and Physics*, 8, 5221-5244, 2008.
783
784



785 **Appendix.**

786

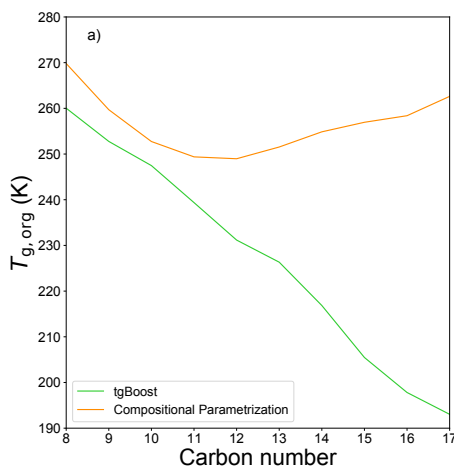
787 **Table A1:** Experimental and simulated functional group distributions, O:C and N:C ratios of
788 SOA generated from C16 oxidation by OH in presence of high NO_x.

FG/C16 molecule	Experimental	Simulated (tgBoost)	Simulated (CP)
Nitrate	0.91	0.65	0.54
Carbonyl	0.38	0.26	0.15
Hydroxyl	0.41	0.43	0.45
Carboxyl	0.09	0.0	0.0
Ester	0.28	0.2	0.07
Peroxide	0.12	0.01	0.0
Methylene	13.81	12.12	12.07
O:C	0.28	0.25	0.25
N:C	0.06	0.04	0.03
H:C	1.85	/	/
MW	294	/	/
Density (g cm ⁻³)	1.10	1.06	1.06

789

790

791



792

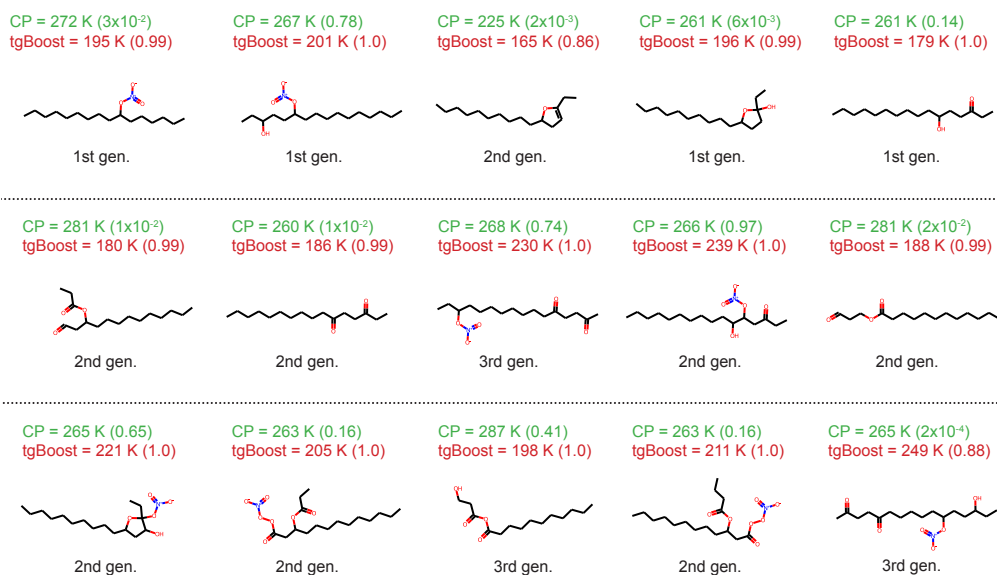
793

794

795

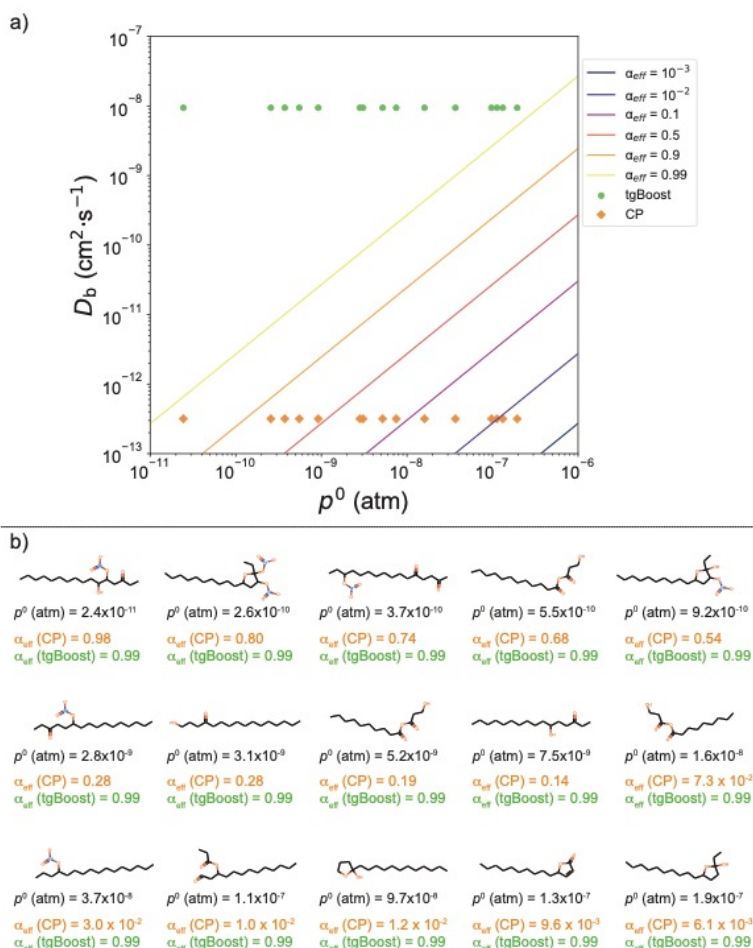
796

Figure A1: Predicted $T_{g,org}$ of SOA generated from n-alkanes as computed by the GECKO-A box model with the T_g compositional parametrization (orange line) and tgBoost (green line) at the last step of the simulations ($t = 3600$ s).



797
798
799
800
801
802
803
804
805

Figure A2. Top 15 species with highest concentrations in oxidation products of n-hexadecane ($C_{16}H_{34}$) under high NO_x conditions simulated by GECKO-A with effective mass accommodation coefficient (α_{eff}) with the compositional parameterization. The species are reported in descending concentrations from left to right and from top to bottom. Listed values are T_g as calculated by tgBoost and CP and α_{eff} values at the end of simulation (3600 s) in brackets. Types of compounds are also noted (1st, 2nd, and 3rd generation products, decomposition products).



806

807 **Figure A3.** a) α_{eff} isolines as a function of bulk diffusivity D_b and saturation vapor pressure
 808 p^0 of semi-volatile species. b) Selection of various representative SOA contributors produced
 809 during the oxidation of n-hexadecane. The species are ordered by decreasing vapor pressure.
 810 The reported α_{eff} values for each SOA contributor are calculated for D_b estimated with tgBoost
 811 ($D_b = 1 \times 10^{-8}$ cm² s⁻¹) and CP ($D_b = 3 \times 10^{-13}$ cm² s⁻¹). The values of α_{eff} for the selected species
 812 are reported as points in the top panel. It shows that for the liquid-like state estimated with the
 813 tgBoost configuration, α_{eff} tend towards 1 for all species. This behavior is not observed in the
 814 amorphous semi-solid state estimated using the CP model configuration for species with p^0
 815 above 10⁻⁹ atm. For the simulated conditions, species with p^0 between 10⁻⁸ and 10⁻⁶ atm are of
 816 enough low volatility to partition between the particle and gas phases at equilibrium. For species
 817 in that volatility range, no mass transfer limitation is observed with the tgBoost configuration,
 818 unlike the CP configuration. Using the CP configuration, the most volatile SOA contributors
 819 are subjected to substantial mass transfer limitation and are therefore mainly eliminated by gas-
 820 phase oxidation or wall deposition.
 821